Enhancing Oxygen Evolution Reaction Activity by Using Switchable Polarization in Ferroelectric $InSnO_2N$

Zhenyun Lan[a], Didrik René Småbråten[b], Chengcheng Xiao[c], Tejs Vegge[a], Ulrich Aschauer[b,*] and Ivano E. Castelli[a,*]

[a] Department of Energy Conversion and Storage, Technical University of Denmark, DK-2800 Kgs. Lyngby, Denmark
[b] Department of Chemistry, Biochemistry and Pharmaceutical Sciences, University of Bern, Bern CH-3012, Switzerland
[c] Departments of Materials and Physics, and the Thomas Young Centre for Theory and Simulation of Materials, Imperial College London, London SW7 2AZ, United Kingdom

* Corresponding Authors
Email: ivca@dtu.dk
Email: ulrich.aschauer@dcb.unibe.ch

Abstract

Ferroelectric modulation of the surface charge density is a promising strategy to promote the surface oxygen evolution reaction (OER) in photocatalytic water splitting. The limitations of the Sabatier principle could be overcome by tuning the interaction strength between the OER intermediates and the surface for the individual reaction steps via switching of the polarization direction. $InSnO_2N$, a newly reported improper ferroelectric semiconductor, is promising for applications as a photocatalyst due to its direct band gap of 1.61 eV and its sizable ferroelectric polarization. Therefore, in this work, we use density functional theory (DFT) to investigate the OER performance on its (001) surface as a function of the bulk polarization direction. We find that the clean surface of the downward (negatively) polarized bulk structure ("polarized bulk" henceforth) has a lower theoretical overpotential of η = 0.58 V vs the standard hydrogen electrode (SHE) compared to the clean surface with an upward (positively) polarized bulk structure (0.77 V). Under (photo)-electrochemical operating conditions, a monolayer (ML) OH

covered surface is the most stable for the negatively polarized bulk and shows a theoretical overpotential of 0.89 V, whereas for the positively polarized bulk structure, a surface covered with 2/3 ML OH is the most stable, also showing an overpotential of 0.89 V. Notably, when switching the polarization direction during the reaction, the overpotential becomes as small as 0.20 V for the clean surface and 0.23 V for the surface with OH coverage, which is far below the usual minimum theoretical overpotential for oxides (η = 0.37 V). We show that the reduction in reaction free energy by ferroelectric switching can be performed in a relevant frequency range and outweighs the energetic cost for polarization switching by a factor 6 to 12. Our study demonstrates that switching of improper ferroelectricity is a highly promising route to boost the OER activity of oxynitride photocatalytic water splitting electrodes.

Keywords: ferroelectric polarization, density functional theory, oxygen evolution reaction, overpotential, $InSnO_2N$

Introduction

Photoferroic materials that combine ferroelectric and light-harvesting properties, are promising for optoelectronic applications, like photovoltaics[1,2] or photo(electro)chemical water-splitting (PEC).[3] The spontaneous polarization of ferroelectrics can be reversed by application of an external electric field, with potential benefits for photoelectrocatalytic water splitting.[4–7] Due to the strong internal electric field induced by the spontaneous electric polarization, the photogenerated electrons and holes migrate in opposite directions, which enhances charge-carrier separation and promotes photocatalytic properties.[8,9] To date, more than 700 ferroelectric materials have been discovered,[10] the majority of those studied for

photoelectrocatalytic applications are complex oxides, such as perovskite oxides, $BiFeO_3$,[11] $PbTiO_3$[12,13] and $BaTiO_3$.[14,15] However, their band gaps are in the ultraviolet (UV) range, they are therefore unable to absorb visible light. Although ferroelectricity could suppress the recombination of photo-induced carriers, the large band gap of these oxides will inhibit practical photocatalytic applications. To solve this, the methods like substitution of one or more oxygen by nitrogen which leads to the so-called oxynitrides has been proposed.[16,17] Compared to oxygen, the lower electronegativity of nitrogen results in reduced band gaps and higher valence band edges that better match the water redox levels.[18–20] Recently, a tin oxynitride-based semiconductor, $InSnO_2N$, was suggested as a new and promising photocatalyst. It has a direct band gap of approx. 1.61 eV, resulting in excellent light absorption.[21] $InSnO_2N$ (Figure 1a) is isostructural to the multiferroic hexagonal manganites, h-$RMnO_3$ (R=Y, In, Sc, Ho-Lu). These materials are improper ferroelectrics, in which the corner-sharing Mn-O trigonal bipyramids are separated by layers of R ions and the tilting of the corner-sharing Mn-O trigonal bipyramids leads to the "up-down-down" R-cation displacement along c axis (or [001]) that causes polarization as a secondary effect and promotes separation of photoexcited carriers.[22,23] In addition to light absorption and carrier separation, the performance of $InSnO_2N$ in a photoelectrochemical device, will depend on its surface redox reaction properties,[24] which are currently unknown. The major obstacle among the water-splitting redox reactions, is the low efficiency of the oxygen evolution reaction (OER).[25–27] The OER is a multistep reaction involving several intermediates and every step is vital for the overall conversion efficiency.[28,29] The interaction between catalyst surface and intermediate, strong or weak, will directly affect the reaction activity. According to the Sabatier principle, if the interaction is too weak, the

adsorbate (i.e. the reagent) will be unable to bind to the catalyst, while if the interaction is too strong, the reaction product will fail to desorb.[30,31] Consequently, an optimal binding strength corresponds to the maximum OER efficiency and a minimum theoretical overpotential. DFT calculations have demonstrated that the four-step OER mechanism is fundamentally limited to a minimum theoretical overpotential of 0.3-0.4 V, due to the scaling relation between the binding strength of the OH and OOH intermediates.[32,33] The adsorption strength between the catalyst and intermediate largely depends on the surface electronic states. In a ferroelectric material, the surface states and their occupation could be altered by switching the polarization direction.[34–37] Recently, the polarization switching of ferroelectric materials have been demonstrated to effectively control the CO_2 reduction.[38,39] Therefore, for a given surface, switching of the polarization direction can also be used to optimize the adsorption strength for intermediates along the OER pathways, overcoming the limit imposed by the Sabatier principle.[40]

In this work, we have used DFT calculations to investigate the OER performance of $InSnO_2N$ surfaces with negatively/positively polarized bulk. We find that the clean surface with a downward (negatively) polarized bulk has a lower theoretical overpotential of 0.58 V vs SHE than the clean surface with an upward (positively) polarized bulk (0.77 V). Under (photo)-electrochemical operating conditions, for the negatively polarized bulk, a 1 monolayer (ML) OH covered surface is the most stable while for the positively polarized bulk, a 2/3 ML OH coverage is preferred. The overpotentials for the OER on the OH covered surfaces with negatively and positively polarized bulk are both 0.89 V. When the polarization direction is switched during the OER, a much lower theoretical overpotential of 0.20 V is achieved for the

clean surface and 0.23 V for the surface with OH coverage. These values are far below the minimum theoretical overpotential for oxides (0.37 V),[33] demonstrating that improper ferroelectric switching of suitable-band gap photoelectrodes is an exciting route to boost the OER activity, the enhancement in reaction free energies outweighing the energetic cost for polarization switching by a factor 6-12.

Method

Computational Methodology

DFT calculations were performed with the Vienna Ab initio Simulation Package (VASP).[41–43] Exchange and correlation effects were described using the Perdew–Burke–Ernzerhof (PBE) functional, in the framework of the generalized gradient approximation (GGA).[44] We used projector augmented wave (PAW)[45] potentials to represent the frozen core electrons and nuclei of each atom, and In (5s, 5d, 5p), Sn (5s, 4d, 5p), O (2s, 2p), and N(3s, 3p) were described as valence electrons, with a plane wave cutoff energy of 520 eV. We used a 6 × 6 × 3 Γ-centered Monkhorst Pack k-point mesh[46] for the bulk unit cell (30 atoms) and a 6 × 6 × 1 mesh for slab models (66 atoms). For the calculations of the partial density of states (PDOS), we used a Γ-centered k-point mesh with 12 × 12 × 6 for the bulk unit cell and 12 × 12 × 1 for the slab. The slab model is composed of 9 atomic layers where the bottom 4 layers are kept fixed during relaxation, a 20 Å vacuum was added to avoid artificial interaction between periodic images and a dipole correction was included.[47] Grimme's D3-correction was used to account for van der Waals interactions.[48] The spontaneous polarization was calculated according to the Born effective charge method,[49] where the Born effective charges are derived within Density

Functional Perturbation Theory (DFPT).[50] All atoms were fully relaxed during the structural optimization until the force on each atom was less than 0.02 eV/Å. The band gap was determined using the HSE06[51] hybrid functional with a plane wave cutoff of 350 eV and a 6 × 6 × 3 Γ-centered k-point mesh. We studied the OER at standard conditions (T = 298.15 K, P = 1 bar, pH = 0), within the computational standard hydrogen electrode (SHE) framework, by considering a widely used mechanism that consists of four proton-coupled electron-transfer (PCET) steps (see *OER mechanism*, Supporting Information).[33,52] The Pourbaix diagram gives information regarding the stability against dissolved phases, ions and chemical reactions with water.[53] The detailed calculation method is explained in ref 50. All data are stored and freely available in the DTU Data Repository.[54]

Results and discussion

The $InSnO_2N$ structure studied in this work is hexagonal and belongs to the polar space group $P6_3cm$, as shown in Figure 1a. The optimized lattice constants are a=b=6.16 Å, c=12.24 Å. The distortion of the Sn-O-N trigonal bipyramids leads to an "up-down-down" corrugation of the In cations along c axis (or [001]) with a polarization of 12.04 μC/cm^2, analogous to the improper ferroelectricity in the hexagonal manganites.[22,55] During ferroelectric switching, the structure goes through a centrosymmetric phase ($P\bar{3}c1$) shown in Figure S1. Therefore, the energy difference between the non-polar $P\bar{3}c1$ and the polar $P6_3cm$ structures (Figure 1c) is calculated to evaluate the energy barrier for polarization switching. We find an energy difference of 5.50 meV/atom, which is close to the switching energy barrier calculated for $YMnO_3$ (5 meV/atom),[56,57] but much smaller than that for $BaTiO_3$ (28 meV/atom),[58] indicating that the polarization in $InSnO_2N$ can be switched using electric fields. The stability of $InSnO_2N$

in the solution has also been analyzed in the Pourbaix diagram in Figure 1b. The yellow zone represents that $InSnO_2N$ is stable under a broad range of potential and pHs, corresponding to the working OER conditions. $InSnO_2N$ can be stable even at the highly acidic/alkaline condition. To evaluate the light absorption properties, we calculate the band structure of bulk $InSnO_2N$ using HSE06: the polar phase $InSnO_2N$ is a direct semiconductor with band gap of 1.61 eV where both the valence band maximum (VBM) and the conduction band minimum (CBM) are located at the Γ point (Figure 1c). The suitable band gap and direct transition are desirable to absorb a large fraction of solar light. As for the non-polar phase, the band gap is 1.45 eV (Figure S2) which is slightly smaller than the polar one.

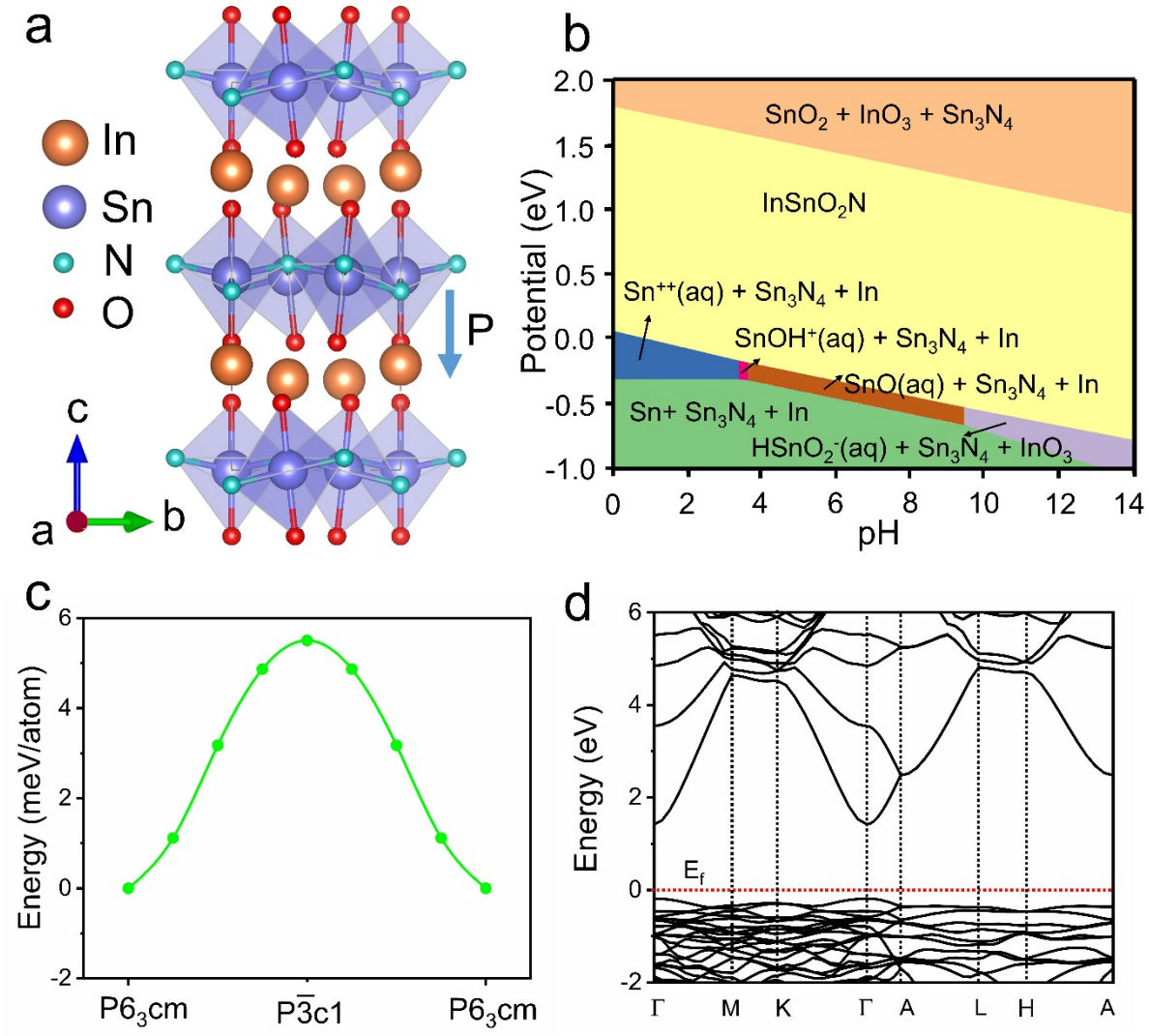

Figure 1. (a) Structure of bulk $InSnO_2N$ with $P6_3cm$ space group. The arrow represents the polarization direction. (b) Theoretical Pourbaix diagram for $InSnO_2N$. The diagrams are drawn for a concentration of 10^{-6} M at 25 °C. (c) Energy barrier of $InSnO_2N$ during through the centrosymmetric $P\bar{3}c1$ phase. (d) HSE06 band structure of bulk $InSnO_2N$ with $P6_3cm$ (polar) space group.

Changes in polarization direction perpendicular to the surface could be used to modulate the surface properties.[37] As the polarization in $InSnO_2N$ lies along the [001] direction, we study the

OER on the (001) surface. The (001) facet has two terminations, SnN and InO_2. To determine which termination is more stable, we calculate surface energies[59,60] of 1.45 J/m^2 and 1.68 J/m^2, for the SnN and InO_2 terminations respectively and consequently investigate the OER on the more stable SnN termination. After surface relaxation, the In corrugations remain "up-down-down" for the slab with negatively polarized bulk (Figure 2a) and "down-up-up" for the slab with positively polarized bulk (Figure 2d). It should be noted that the polarization in each layer is highly dependent on the paraelectric reference state used to calculate the polarization. When the unrelaxed centrosymmetric phase is used as reference, all relaxed layers have a negative polarization for the nominally negatively polarized slab (Figure S3b). On the other hand, for the positively polarized slab, due to the surface relaxation, there is an effective reversal of the polarization in the first three layers, as shown in Figure S3e, despite the fact that the In corrugation does not change. When the relaxed centrosymmetric phase is used as reference, only the first subsurface layer in the negatively polarized slab has a small positive polarization (Figure S3c) and only the surface layer in the positively polarized slab has a small negative polarization (Figure S3f). Since the In corrugation is retained, we believe that relaxations of the interlayer spacing and interlayer rumpling are responsible for the subtle local changes in the sign of the polarization. We investigate the electronic structure for the two slabs with oppositely polarized bulk. From the layer-resolved partial density of states (Figure 2), there is a positive shift of the Fermi level for the surface with positively polarized bulk compared to the surface with negative polarization direction, which implies electrons transfer to the surface. This is also confirmed by the Bader analysis (see Table S2), which shows that the charge on positively polarized surface is 0.16 electrons higher than the charge on the negatively polarized

surface.

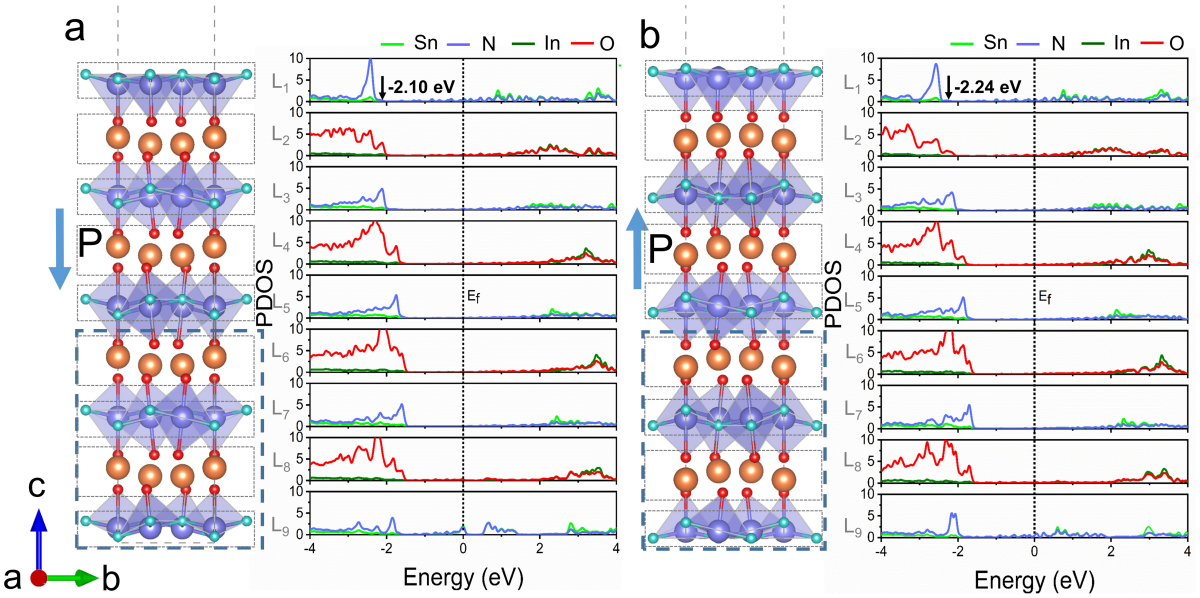

Figure 2. Structures and layer-resolved partial density of states (PDOS) of the $InSnO_2N$ (001) surface with (a) negatively polarized bulk and (b) positively polarized bulk. The arrow represents the polarization direction. L_n (1, 2, 3…9) corresponds to the atomic layer of the left structure. The bottom four-layer atoms marked by the dashed rectangle are fixed during the optimization.

To study the effect of the polarization on the OER activity, we first calculate free energy differences for the reaction steps on the clean (without adsorbates) (001) surface with oppositely polarized bulk. From the free energy profile of the OER in Figure 3, we find that for the surface with a negatively polarized bulk, the potential determining step is the formation of O, resulting in a theoretical overpotential of 0.58 V. For the surface with a positive bulk polarization, the binding energies of the adsorbates are more negative as shown in Table 1, since the adsorption strength between the adsorbates and surface is related to the surface electronic properties and there is the higher electron density on the surface with positively

polarized bulk. The potential determining step also changes to the formation of OOH and results in a theoretical overpotential of 0.77 V.

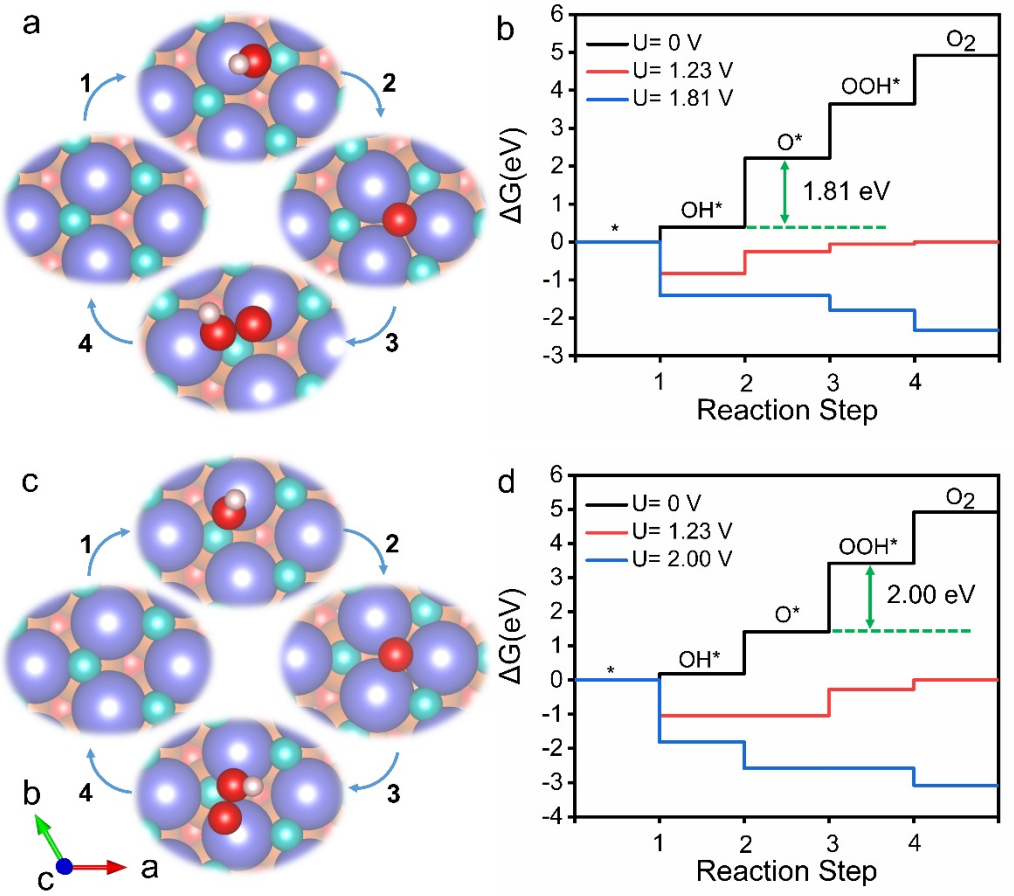

Figure 3. (a) OER steps and (b) Gibbs free energy diagram for the clean $InSnO_2N$ (001) surface with negatively polarized bulk. (c) OER steps and (d) Gibbs free energy diagram for the clean $InSnO_2N$ (001) surface with positively polarized bulk. Color code: In=orange, Sn= violet, O= red, N= cyan, H=pale pink.

Table 1. Calculated Gibbs adsorption free energies of the three OER intermediates on the (001) surface with negatively/positively polarized bulk.

	ΔG_{OH^*} (eV)	ΔG_{O^*} (eV)	ΔG_{OOH^*} (eV)
Surface with negatively polarized bulk	0.40	2.21	3.64
Surface with positively polarized bulk	0.19	1.42	3.42

The surface structure changes under OER operating conditions, and we evaluate the stable adsorbate coverage via surface Pourbaix diagrams for surfaces with negative and positive bulk polarization at pH=0. In Figure 4a, we see that, for the surface with negatively polarized bulk, at a potential close to zero, the clean surface is the most stable. When the potential is in the range between 0.39 and 1.07 V, the surface prefers to be covered with 1/3 ML OH. In the range of 1.07 to 1.53 V, a 1 ML OH coverage is thermodynamically favored. For higher potentials, the surface prefers to be covered with 1 ML O. For the positively polarized surface (Figure 4b), when the potential is lower than 0.14 V, the clean surface is the most stable. The 1/3 ML OH covered surface becomes the most stable for the potential between 0.14 and 0.72 V. While the most stable surface changes to the 2/3 ML OH covered surface for the potential in the range of 0.72-1.71 V. When the potential is higher than 1.71 V, the surface prefers to be covered with 2/3 ML O.

As the working potential of the photocatalyst is determined by the energy difference between the VBM and the SHE, we evaluate the position of valence band edge of bulk $InSnO_2N$ with respect to the SHE as 1.89 eV via an empirical method.[61–63] The band edges of the various surfaces have further been evaluated by aligning the DOS of bulk $InSnO_2N$ and its surfaces at In 1s states. For the surface with negatively polarized bulk, the estimated surface VBM is 1.26 eV vs SHE and the surface is covered with 1 ML OH at this potential. For the surface with positively polarized bulk, the estimated surface VBM is 1.39 eV vs SHE and, as shown in Figure 4b, the surface is covered with 2/3 ML OH at this potential. From our calculation results, we find that when an electric field of 0.05 V/Å is applied, the VBM position of the estimated

surface vs the water redox levels doesn't change.

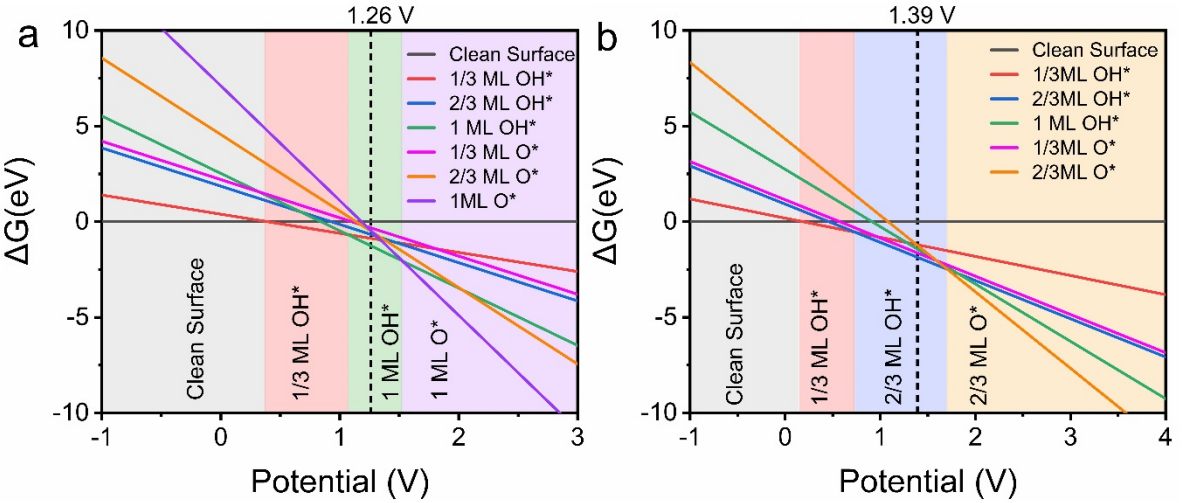

Figure 4. Surface Pourbaix diagrams of the SnN terminated (001) surface at pH=0 with (a) negatively polarized bulk and (b) positively polarized bulk. The dashed lines represent the redox potential of the photogenerated holes.

When OER happens on the 1 ML OH covered surface with negatively polarized bulk, as shown in Figure 5a, there are two possible OH positions, one on top of a Sn atom and the other on top of an N atom. We find that the OER is more facile when started from the OH on top of the Sn atoms. The free energy diagram (Figure 5b) reveals that the potential determining step is the formation of OOH with a free energy change of 2.12 eV, corresponding to a fairly large theoretical overpotential of 0.89 V.

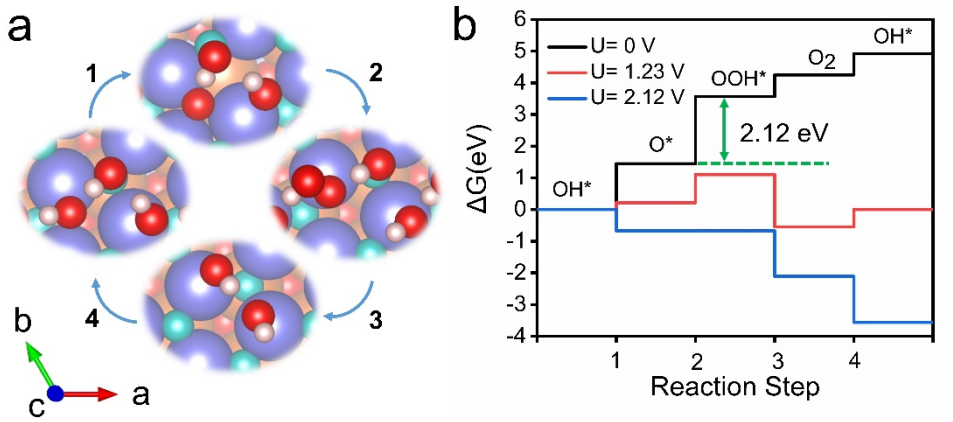

Figure 5. (a) OER steps and (b) Gibbs free energy diagram for the 1 ML OH* covered $InSnO_2N$ (001) surface with negatively polarized bulk.

Unlike on the negatively polarized one, the OER on the 2/3 ML OH* covered surface with positively polarized bulk has two possible paths. As shown in Figure 6a-b, the OER starting from an OH, proceeding in a similar fashion to the negatively polarized bulk, requires a theoretical overpotential of 0.89 V. On the other hand, as shown in Figure 6c-d, the OER can also start via the deprotonation of one H_2O molecule on the top site of the Sn atom. Interestingly the OOH fragment is unstable on top of the Sn and will spontaneously dissociate into two O fragment adsorbed on top of the Sn, while H binds to OH on a neighboring site to form H_2O bound to a Sn atom. In this mechanism, the potential determining step is the formation of two O fragment which corresponds to a change in free energy of 2.27 eV, corresponding to a much higher theoretical overpotential of 1.04 V.

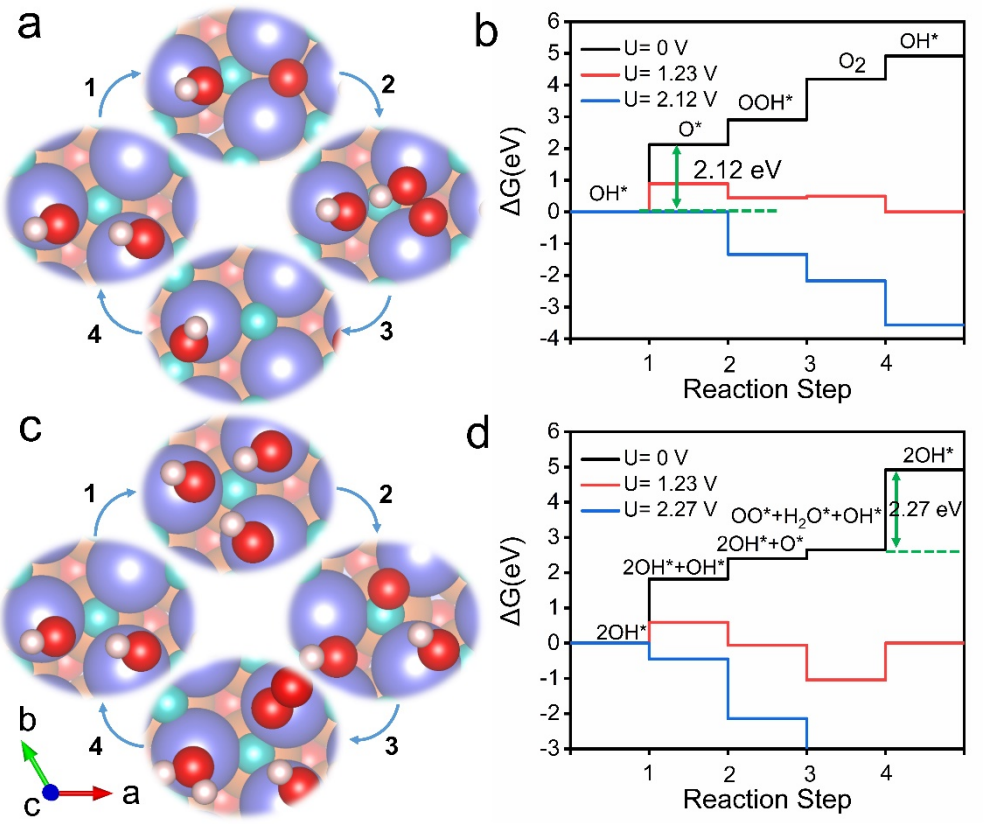

Figure 6. (a) OER steps and (b) Gibbs free energy diagram for the 2/3 ML OH* covered $InSnO_2N$ (001) surface with positively polarized bulk considering OH* as starting site. (c) OER steps and (d) Gibbs free energy diagram for the 2/3 ML OH* covered $InSnO_2N$ (001) surface with positively polarized bulk considering the top of Sn top site as starting site.

Based on the above, neither of the two polarization directions alone are particularly promising for OER. However, the different potentials determining steps for surfaces with opposite bulk polarization suggest that switching of the polarization direction could be used to enhance the OER activity. Such an enhanced pathway on the clean surface is shown in Figure 7a, where first, one H_2O molecule is deprotonated, leading to an OH fragment adsorbed on the surface with negatively polarized bulk. Then the polarization direction is switched and the OH fragment is adsorbed on the surface with positive polarization before being deprotonated to O.

Afterwards the polarization direction is switched again to negative and a deprotonated H_2O molecule associates with the O to form an OOH on the surface. The OOH is then deprotonated and forms an O_2 molecule that leaves from the surface in step 4. The potential determining step of this process is the formation of OOH with a free energy change of 1.43 eV, corresponding to a theoretical overpotential of only 0.20 V. The theoretical overpotential is largely decreased, compared to that of the clean surface with negatively (0.58 V) or positively (0.77 V) polarized bulk.

Under operating condition, the change of the bulk polarization direction could also be useful to enhance the OER activity. As shown in Figure 7b, in step 1, for the 1ML OH covered surface with negatively polarized bulk, the OER happens on one of the OH, which is deprotonated to O. The polarization direction can then be changed to positive. In this state a sub-ML coverage of OH is preferred and we assume that one OH desorbs from the surface and then forms OOH with the O adsorbate. This OOH is then deprotonated and desorbs as O_2 before the OH coverage is restored after a further polarization switch. This OER process is limited by the formation of OOH and the potential needed for all steps to be downhill is 1.46 V, which corresponds to a theoretical overpotential of only 0.23 V.

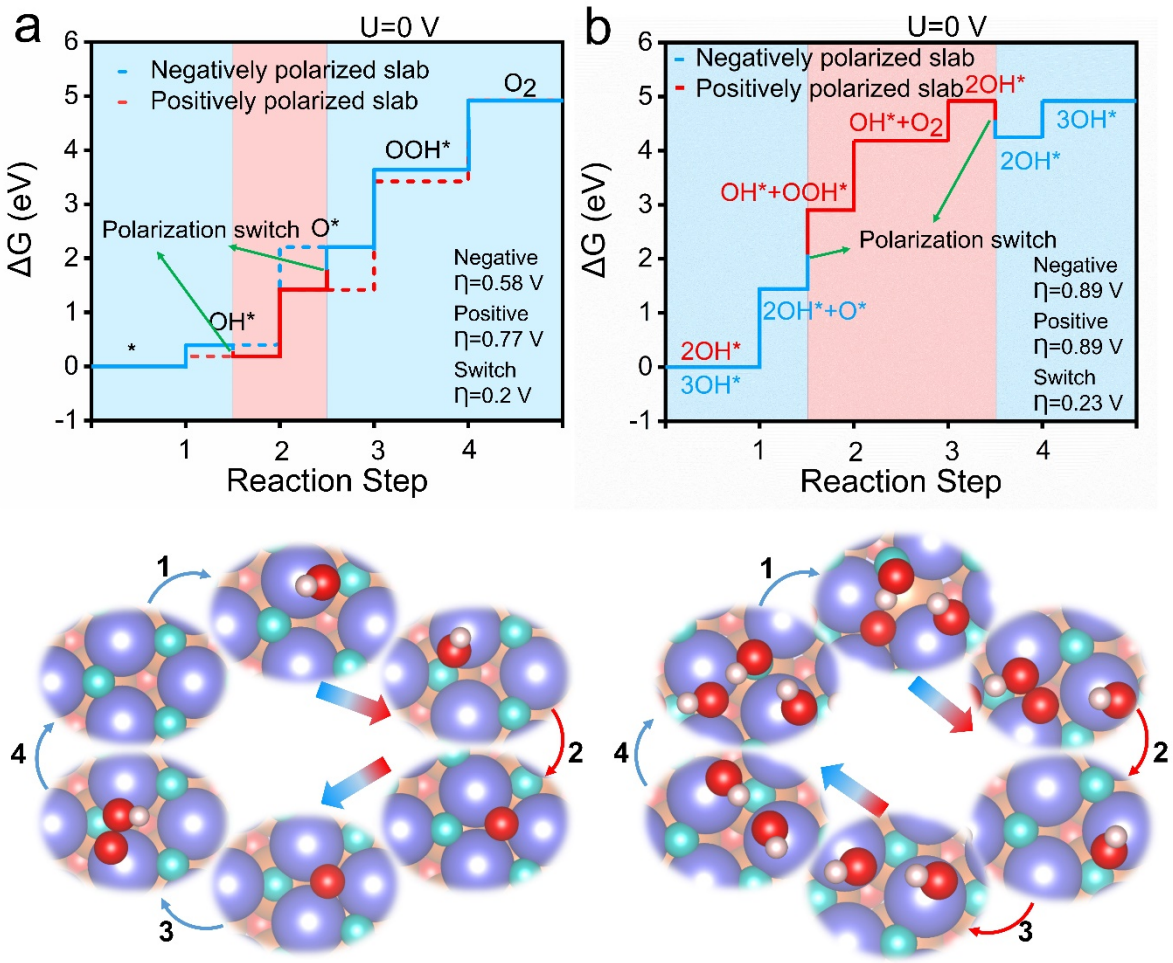

Figure 7. Gibbs free energy diagrams and OER steps including polarization switching for (a) the clean $InSnO_2N$ (001) surface and (b) the OH* covered $InSnO_2N$ (001) surface. The arrows indicate switching of the polarization direction.

The above enhancement of the OER activity relies on switching the polarization direction twice throughout the catalytic cycle, which is associated with an energetic cost. Based on the data in Figure 1b, switching amounts to an energetic cost of 5.5 meV/atom or 27.5 meV per formula unit having one Sn reactive site. During one OER cycle we thus need to provide 55 meV for the switching. We note that this analysis considers homogeneous switching of the ferroelectric, whereas a domain-mediated mechanism usually leads to a smaller energetic cost in non-2D or

ultrathin ferroelectrics.[64] We also neglect the fact that surface adsorbates will slightly affect the switching barrier but expect this effect to cancel to a large extent for the two polarization switches, since one barrier will increase, while the one of the reverse switch is decreased.[65] Despite these approximations, we expect the above estimation to yield a good upper-bound estimate of the involved energetic costs. One performance metric for a dynamic switched catalyst is the thermodynamic efficiency,[66] defined in our case as the ratio of the free-energy change of the largest OER step and the energetic cost of the ferroelectric switching, i.e. (0.58 eV - 0.20 eV) / 0.055 eV = 6.9 for the clean surface and (0.89 eV – 0.23 eV) / 0.055 eV = 12 for the adsorbate covered surface, respectively. These ratios show that the reduction of the OER free energy profile by far outweighs the cost for polarization switching. Enhanced turnover frequencies compared to the steady state represent another possible switching-frequency dependent performance metric for dynamic catalysts,[66] which unfortunately are not readily available in our thermochemical DFT framework. Nevertheless, we note that ferroelectric hexagonal manganite oxides such as $ErMnO_3$, were shown to be switchable in a frequency range from 0.1 to 1000 Hz,[67] which covers the optimally resonant range for typical catalytic reactions such as formic acid oxidation[68] and should allow the practical implementation of switched $InSnO_2N$ ferroelectric photocatalysts. Moreover, it is also suitable for the large-scale catalyst with numerous active sites, even though the reaction steps of each active site are not usually synchronized. However, when the overpotential is larger than the needed value, the reaction will stop, and the fragments will “pile up”. The reaction will restart when the polarization direction is flipped, which would enable a self-synchronization of the active sites. Meanwhile, we would like to note that the electric field might influence the surface properties

and thus change the energetics of the intermediates. However, a study of the properties of $InSnO_2N$ under different applied electric fields is a natural extension of the present work.

Conclusion

In this work, we have theoretically investigated the effect of surface ferroelectric switching on the OER performance of the improper ferroelectric $InSnO_2N$ by means of DFT calculations. For the clean surface, the surface with negatively polarized bulk has a lower theoretical overpotential of 0.58 V, compared with the surface with positively polarized bulk (0.77 V), which is related to the increased surface electrons density. Under (photo)-electrochemical operating condition, the surface with negatively polarized bulk prefers to be covered with 1 ML OH, while for the positively polarized bulk, the surface covered with 2/3 ML OH is most stable. The theoretical overpotential for the OER on the surface with negative polarized bulk is 0.89 V which is same as the one with positively polarized bulk. When the polarization direction is switched during the OER, a lower theoretical overpotential as low as $\eta = 0.20$ V is observed for the clean surface and 0.23 V for the surface with OH coverage, which is far below the minimum theoretical overpotential for oxides (0.37 V). Moreover the reduction in reaction free energy is larger by a factor 6 to 12 compared to the estimated energetic cost for polarization switching. This suggests that switching the improper ferroelectric polarization direction is a valuable path towards optimizing ferroelectric OER catalysts.

Notes

The authors declare no competing financial interest.

Supporting information

Method details for OER mechanism; structures for bulk $InSnO_2N$; structures and layer-by-layer out of plane spontaneous polarization of the $InSnO_2N$ (001) surface; zero-point-energy corrections; net charge of the atoms on the surface and entropic contributions to free energies.

Acknowledgments

Z.L. and C.X. acknowledge support from the China Scholarship Council (CSC). T.V. wishes to acknowledge the Velux Foundations for financial support through the research center V-Sustain (grant #9455). T.V and I.E.C. acknowledge the support from the Department of Energy Conversion and Storage, Technical University of Denmark, through the Special Competence Initiative "Autonomous Materials Discovery (http://www.aimade.org/)". D.R.S. and U.A. were supported by the Swiss National Science Foundation under projects 200021_178791 and PP00P2_187185 respectively.

References

(1) Butler, K. T.; Frost, J. M.; Walsh, A. Ferroelectric Materials for Solar Energy Conversion: Photoferroics Revisited. *Energy Environ. Sci.* **2015**, *8*, 838–848.

(2) Castelli, I. E.; Olsen, T.; Chen, Y. Towards Photoferroic Materials by Design: Recent Progress and Perspectives. *J. Phys. Energy* **2019**, *2*, 011001.

(3) Kim, S.; Nguyen, N.; Bark, C. Ferroelectric Materials: A Novel Pathway for Efficient Solar Water Splitting. *Appl. Sci.* **2018**, *8*, 1526.

(4) Lee, J. H.; Selloni, A. Ferroelectric Heterostructures as Dynamic Polarization-Promoted Catalysts for Photochemical and Electrochemical Oxidation of Water. *Phys. Rev. Lett.* **2014**, *112*, 196102.

(5) Singh, S.; Sangle, A. L.; Wu, T.; Khare, N.; MacManus-Driscoll, J. L. Growth of Doped $SrTiO_3$ Ferroelectric Nanoporous Thin Films and Tuning of Photoelectrochemical Properties with Switchable Ferroelectric Polarization. *ACS Appl. Mater. Interfaces* **2019**, *11*, 45683–45691.

(6) Yin, X.; Li, X.; Liu, H.; Gu, W.; Zou, W.; Zhu, L.; Fu, Z.; Lu, Y. Realizing Selective Water Splitting Hydrogen/Oxygen Evolution on Ferroelectric Bi_3TiNbO_9 Nanosheets. *Nano Energy* **2018**, *49*, 489–497.

(7) Ju, L.; Shang, J.; Tang, X.; Kou, L. Tunable Photocatalytic Water Splitting by the Ferroelectric Switch in a 2D $AgBiP_2Se_6$ Monolayer. *J. Am. Chem. Soc.* **2020**, *142*, 1492–1500.

(8) Tiwari, D.; Dunn, S. Photochemistry on a Polarisable Semi-Conductor: What Do We Understand Today? *J. Mater. Sci.* **2009**, *44*, 5063–5079.

(9) Li, L.; Salvador, P. A.; Rohrer, G. S. Photocatalysts with Internal Electric Fields. *Nanoscale* **2014**, *6*, 24–42.

(10) Scott, J. F. Applications of Modern Ferroelectrics. *Science (80-.).* **2007**, *315*, 954–959.

(11) Lejman, M.; Vaudel, G.; Infante, I. C.; Gemeiner, P.; Gusev, V. E.; Dkhil, B.; Ruello, P. Giant Ultrafast Photo-Induced Shear Strain in Ferroelectric $BiFeO_3$. *Nat. Commun.* **2014**, *5*, 4301.

(12) Feng, Y.; Xu, M.; Liu, H.; Li, W.; Li, H.; Bian, Z. Charge Separation and Interfacial Selectivity Induced by Synergistic Effect of Ferroelectricity and Piezoelectricity on

$PbTiO_3$ Monocrystalline Nanoplates. *Nano Energy* **2020**, *73*, 104768.

(13) Liu, Y.; Ye, S.; Xie, H.; Zhu, J.; Shi, Q.; Ta, N.; Chen, R.; Gao, Y.; An, H.; Nie, W.; et al. Internal-Field-Enhanced Charge Separation in a Single-Domain Ferroelectric $PbTiO_3$ Photocatalyst. *Adv. Mater.* **2020**, *32*, 1906513.

(14) Senthilkumar, P.; Jency, D. A.; Kavinkumar, T.; Dhayanithi, D.; Dhanuskodi, S.; Umadevi, M.; Manivannan, S.; Giridharan, N. V.; Thiagarajan, V.; Sriramkumar, M.; et al. Built-in Electric Field Assisted Photocatalytic Dye Degradation and Photoelectrochemical Water Splitting of Ferroelectric Ce Doped $BaTiO_3$ Nanoassemblies. *ACS Sustain. Chem. Eng.* **2019**, *7*, 12032-12043.

(15) Cui, Y.; Briscoe, J.; Dunn, S. Effect of Ferroelectricity on Solar-Light-Driven Photocatalytic Activity of $BaTiO_3$ —Influence on the Carrier Separation and Stern Layer Formation. *Chem. Mater.* **2013**, *25*, 4215–4223.

(16) Fuertes, A. Metal Oxynitrides as Emerging Materials with Photocatalytic and Electronic Properties. *Mater. Horizons* **2015**, *2*, 453-461.

(17) Siritanaratkul, B.; Maeda, K.; Hisatomi, T.; Domen, K. Synthesis and Photocatalytic Activity of Perovskite Niobium Oxynitrides with Wide Visible-Light Absorption Bands. *ChemSusChem* **2011**, *4*, 74–78.

(18) Kasahara, A.; Nukumizu, K.; Takata, T.; Kondo, J. N.; Hara, M.; Kobayashi, H.; Domen, K. $LaTiO_2N$ as a Visible-Light (≤600 nm)-Driven Photocatalyst (2). *J. Phys. Chem. B* **2003**, *107*, 791–797.

(19) Aguiar, R.; Logvinovich, D.; Weidenkaff, A.; Rachel, A.; Reller, A.; Ebbinghaus, S. G. The Vast Colour Spectrum of Ternary Metal Oxynitride Pigments. *Dye. Pigment.* **2008**, *76*, 70–75.

(20) Castelli, I. E.; Olsen, T.; Datta, S.; Landis, D. D.; Dahl, S.; Thygesen, K. S.; Jacobsen, K. W. Computational Screening of Perovskite Metal Oxides for Optimal Solar Light Capture. *Energy Environ. Sci.* **2012**, *5*, 5814–5819.

(21) Hartman, S. T.; Thind, A. S.; Mishra, R. Tin Oxynitride-Based Ferroelectric Semiconductors for Solar Energy Conversion Applications. *Chem. Mater.* **2020**, *32*, 9542–9550.

(22) Van Aken, B. B.; Palstra, T. T. M.; Filippetti, A.; Spaldin, N. A. The Origin of

Ferroelectricity in Magnetoelectric $YMnO_3$. *Nat. Mater.* **2004**, *3*, 164–170.

(23) Skjærvø, S. H.; Meier, Q. N.; Feygenson, M.; Spaldin, N. A.; Billinge, S. J. L.; Bozin, E. S.; Selbach, S. M. Unconventional Continuous Structural Disorder at the Order-Disorder Phase Transition in the Hexagonal Manganites. *Phys. Rev. X* **2019**, *9*, 031001.

(24) Li, Y.; Li, J.; Yang, W.; Wang, X. Implementation of Ferroelectric Materials in Photocatalytic and Photoelectrochemical Water Splitting. *Nanoscale Horizons* **2020**, *5*, 1174–1187.

(25) Li, L.; Wang, P.; Shao, Q.; Huang, X. Recent Progress in Advanced Electrocatalyst Design for Acidic Oxygen Evolution Reaction. *Adv. Mater.* **2021**, 2004243.

(26) Rao, R. R.; Kolb, M. J.; Giordano, L.; Pedersen, A. F.; Katayama, Y.; Hwang, J.; Mehta, A.; You, H.; Lunger, J. R.; Zhou, H.; et al. Operando Identification of Site-Dependent Water Oxidation Activity on Ruthenium Dioxide Single-Crystal Surfaces. *Nat. Catal.* **2020**, *3*, 516–525.

(27) Yang, C.; Rousse, G.; Louise Svane, K.; Pearce, P. E.; Abakumov, A. M.; Deschamps, M.; Cibin, G.; Chadwick, A. V.; Dalla Corte, D. A.; Anton Hansen, H.; et al. Cation Insertion to Break the Activity/Stability Relationship for Highly Active Oxygen Evolution Reaction Catalyst. *Nat. Commun.* **2020**, *11*, 1378.

(28) Rossmeisl, J.; Qu, Z.-W.; Zhu, H.; Kroes, G.-J.; Nørskov, J. K. Electrolysis of Water on Oxide Surfaces. *J. Electroanal. Chem.* **2007**, *607*, 83–89.

(29) Kim, J. S.; Kim, B.; Kim, H.; Kang, K. Recent Progress on Multimetal Oxide Catalysts for the Oxygen Evolution Reaction. *Adv. Energy Mater.* **2018**, *8*, 1702774.

(30) Nørskov, J. K.; Bligaard, T.; Rossmeisl, J.; Christensen, C. H. Towards the Computational Design of Solid Catalysts. *Nat. Chem.* **2009**, *1*, 37–46.

(31) Vonrüti, N.; Aschauer, U. Catalysis on Oxidized Ferroelectric Surfaces—Epitaxially Strained $LaTiO_2N$ and $BaTiO_3$ for Photocatalytic Water Splitting. *J. Chem. Phys.* **2020**, *152*, 024701.

(32) Koper, M. T. M. Thermodynamic Theory of Multi-Electron Transfer Reactions: Implications for Electrocatalysis. *J. Electroanal. Chem.* **2011**, *660*, 254–260.

(33) Man, I. C.; Su, H.; Calle-Vallejo, F.; Hansen, H. A.; Martínez, J. I.; Inoglu, N. G.; Kitchin, J.; Jaramillo, T. F.; Nørskov, J. K.; Rossmeisl, J. Universality in Oxygen

Evolution Electrocatalysis on Oxide Surfaces. *ChemCatChem* **2011**, *3*, 1159–1165.

(34) Dues, C.; Schmidt, W. G.; Sanna, S. Water Splitting Reaction at Polar Lithium Niobate Surfaces. *ACS Omega* **2019**, *4*, 3850–3859.

(35) Kakekhani, A.; Ismail-Beigi, S. Polarization-Driven Catalysis via Ferroelectric Oxide Surfaces. *Phys. Chem. Chem. Phys.* **2016**, *18*, 19676–19695.

(36) Kakekhani, A.; Ismail-Beigi, S. Ferroelectric-Based Catalysis: Switchable Surface Chemistry. *ACS Catal.* **2015**, *5*, 4537-4545.

(37) Garrity, K.; Kakekhani, A.; Kolpak, A.; Ismail-Beigi, S. Ferroelectric Surface Chemistry: First-Principles Study of the $PbTiO_3$ Surface. *Phys. Rev. B* **2013**, *88*, 045401.

(38) Yu, H.; Chen, F.; Li, X.; Huang, H.; Zhang, Q.; Su, S.; Wang, K.; Mao, E.; Mei, B.; Mul, G.; et al. Synergy of Ferroelectric Polarization and Oxygen Vacancy to Promote CO_2 Photoreduction. *Nat. Commun.* **2021**, *12*, 4594.

(39) Ju, L.; Tan, X.; Mao, X.; Gu, Y.; Smith, S.; Du, A.; Chen, Z.; Chen, C.; Kou, L. Controllable CO_2 Electrocatalytic Reduction via Ferroelectric Switching on Single Atom Anchored In_2Se_3 Monolayer. *Nat. Commun.* **2021**, *12*, 5128.

(40) Wan, T. L.; Ge, L.; Pan, Y.; Yuan, Q.; Liu, L.; Sarina, S.; Kou, L. Catalysis Based on Ferroelectrics: Controllable Chemical Reaction with Boosted Efficiency. *Nanoscale* **2021**, *13*, 7096–7107.

(41) Kresse, G.; Hafner, J. Ab Initio Molecular Dynamics for Liquid Metals. *Phys. Rev. B* **1993**, *47*, 558–561.

(42) Kresse, G.; Furthmüller, J. Efficient Iterative Schemes for Ab Initio Total-Energy Calculations Using a Plane-Wave Basis Set. *Phys. Rev. B* **1996**, *54*, 11169–11186.

(43) Kresse, G.; Furthmüller, J. Efficiency of Ab-Initio Total Energy Calculations for Metals and Semiconductors Using a Plane-Wave Basis Set. *Comput. Mater. Sci.* **1996**, *6*, 15–50.

(44) Perdew, J. P.; Burke, K.; Ernzerhof, M. Generalized Gradient Approximation Made Simple. *Phys. Rev. Lett.* **1996**, *77*, 3865–3868.

(45) Kresse, G.; Joubert, D. From Ultrasoft Pseudopotentials to the Projector Augmented-Wave Method. *Phys. Rev. B* **1999**, *59*, 1758–1775.

(46) Monkhorst, H. J.; Pack, J. D. Special Points for Brillouin-Zone Integrations. *Phys. Rev.*

B **1976**, *13*, 5188–5192.

(47) Bengtsson, L. Dipole Correction for Surface Supercell Calculations. *Phys. Rev. B* **1999**, *59*, 12301–12304.

(48) Grimme, S.; Antony, J.; Ehrlich, S.; Krieg, H. A Consistent and Accurate Ab Initio Parametrization of Density Functional Dispersion Correction (DFT-D) for the 94 Elements H-Pu. *J. Chem. Phys.* **2010**, *132*, 154104.

(49) Neaton, J. B.; Ederer, C.; Waghmare, U. V.; Spaldin, N. A.; Rabe, K. M. First-Principles Study of Spontaneous Polarization in Multiferroic $BiFeO_3$. *Phys. Rev. B* **2005**, *71*, 014113.

(50) Stefano Baroni; Giannozzi, P.; Testa, A. Green's-Function Approach to Linear Response in Solids Stefano. *Phys. Rev. Lett.* **1987**, *58*, 1100–1103.

(51) Heyd, J.; Scuseria, G. E.; Ernzerhof, M. Hybrid Functionals Based on a Screened Coulomb Potential. *J. Chem. Phys.* **2003**, *118*, 8207–8215.

(52) Valdés, Á.; Qu, Z.-W.; Kroes, G.-J.; Rossmeisl, J.; Nørskov, J. K. Oxidation and Photo-Oxidation of Water on TiO_2 Surface. *J. Phys. Chem. C* **2008**, *112*, 9872–9879.

(53) Castelli, I. E.; Thygesen, K. S.; Jacobsen, K. W. Calculated Pourbaix Diagrams of Cubic Perovskites for Water Splitting: Stability Against Corrosion. *Top. Catal.* **2014**, *57*, 265–272.

(54) DTU Data Repository,Https://Doi.Org/10.11583/DTU.14528670.

(55) Fennie, C. J.; Rabe, K. M. Ferroelectric Transition in $YMnO_3$ from First Principles. *Phys. Rev. B* **2005**, *72*, 100103.

(56) Småbråten, D. R.; Holstad, T. S.; Evans, D. M.; Yan, Z.; Bourret, E.; Meier, D.; Selbach, S. M. Domain Wall Mobility and Roughening in Doped Ferroelectric Hexagonal Manganites. *Phys. Rev. Res.* **2020**, *2*, 033159.

(57) Artyukhin, S.; Delaney, K. T.; Spaldin, N. A.; Mostovoy, M. Landau Theory of Topological Defects in Multiferroic Hexagonal Manganites. *Nat. Mater.* **2014**, *13*, 42–49.

(58) Zhang, Y.; Sun, J.; Perdew, J. P.; Wu, X. Comparative First-Principles Studies of Prototypical Ferroelectric Materials by LDA, GGA, and SCAN Meta-GGA. *Phys. Rev. B* **2017**, *96*, 035143.

(59) Heifets, E.; Eglitis, R. I.; Kotomin, E. A.; Kotomin, E. A.; Maier, J.; Borstel, G. Ab Initio Modeling of Surface Structure for $SrTiO_3$ Perovskite Crystals. *Phys. Rev. B - Condens. Matter Mater. Phys.* **2001**, *64*, 235417.

(60) Eglitis, R. I.; Vanderbilt, D. Ab Initio Calculations of $BaTiO_3$ and $PbTiO_3$ (001) and (011) Surface Structures. *Phys. Rev. B* **2007**, *76*, 155439.

(61) Castelli, I. E.; Landis, D. D.; Thygesen, K. S.; Dahl, S.; Chorkendorff, I.; Jaramillo, T. F.; Jacobsen, K. W. New Cubic Perovskites for One- and Two-Photon Water Splitting Using the Computational Materials Repository. *Energy Environ. Sci.* **2012**, *5*, 9034.

(62) Mulliken, R. S. A New Electroaffinity Scale; Together with Data on Valence States and on Valence Ionization Potentials and Electron Affinities. *J. Chem. Phys.* **1934**, *2*, 782–793.

(63) Bouri, M.; Aschauer, U. Suitability of Different Sr_2TaO_3N Surface Orientations for Photocatalytic Water Oxidation. *Chem. Mater.* **2020**, *32*, 75–84.

(64) Bystrov, V. S.; Fridkin, V. M. Domain and Homogeneous Switching in Ferroelectrics. *Ferroelectrics* **2020**, *569*, 164–181.

(65) Lee, H.; Kim, T. H.; Patzner, J. J.; Lu, H.; Lee, J.-W.; Zhou, H.; Chang, W.; Mahanthappa, M. K.; Tsymbal, E. Y.; Gruverman, A.; et al. Imprint Control of $BaTiO_3$ Thin Films via Chemically Induced Surface Polarization Pinning. *Nano Lett.* **2016**, *16*, 2400–2406.

(66) Shetty, M.; Walton, A.; Gathmann, S. R.; Ardagh, M. A.; Gopeesingh, J.; Resasco, J.; Birol, T.; Zhang, Q.; Tsapatsis, M.; Vlachos, D. G.; et al. The Catalytic Mechanics of Dynamic Surfaces: Stimulating Methods for Promoting Catalytic Resonance. *ACS Catal.* **2020**, *10*, 12666–12695.

(67) Ruff, A.; Li, Z.; Loidl, A.; Schaab, J.; Fiebig, M.; Cano, A.; Yan, Z.; Bourret, E.; Glaum, J.; Meier, D.; et al. Frequency Dependent Polarisation Switching in h-$ErMnO_3$. *Appl. Phys. Lett.* **2018**, *112*, 182908.

(68) Gopeesingh, J.; Ardagh, M. A.; Shetty, M.; Burke, S. T.; Dauenhauer, P. J.; Abdelrahman, O. A. Resonance-Promoted Formic Acid Oxidation via Dynamic Electrocatalytic Modulation. *ACS Catal.* **2020**, *10*, 9932–9942.

TOC